The sea-level budget along the Northwest Atlantic coast
GIA, mass changes, and large-scale ocean dynamics

Frederikse, Thomas; Simon, Karen; Katsman, Caroline A.; Riva, Riccardo

DOI
10.1002/2017JC012699

Publication date
2017

Document Version
Final published version

Published in
Journal Of Geophysical Research-Oceans

AGU PUBLICATIONS

JGR

Journal of Geophysical Research: Oceans

RESEARCH ARTICLE

10.1002/2017JC012699

The sea-level budget along the Northwest Atlantic coast: GIA, mass changes, and large-scale ocean dynamics

Thomas Frederikse[1], Karen Simon[1], Caroline A. Katsman[2], and Riccardo Riva[1]

[1]Department of Geoscience and Remote Sensing, Delft University of Technology, Delft, Netherlands, [2]Department of Hydraulic Engineering, Delft University of Technology, Delft, Netherlands

Key Points:
- We close the sea-level budget along the northwestern Atlantic coast between 1965 and 2015
- Decadal sea-level variability strongly correlated with steric height in Subpolar Gyre
- Observed decadal variability, trend, and acceleration can be explained by mass redistribution and ocean dynamic effects

Supporting Information:
- Supporting Information S1

Correspondence to:
T. Frederikse,
t.frederikse@tudelft.nl

Citation:
Frederikse, T., K. Simon, C. A. Katsman, and R. Riva (2017), The sea-level budget along the Northwest Atlantic coast: GIA, mass changes, and large-scale ocean dynamics, *J. Geophys. Res. Oceans*, *122*, 5486–5501, doi:10.1002/2017JC012699.

Received 12 JAN 2017
Accepted 10 MAY 2017
Accepted article online 16 MAY 2017
Published online 10 JUL 2017

Abstract Sea-level rise and decadal variability along the northwestern coast of the North Atlantic Ocean are studied in a self-consistent framework that takes into account the effects of solid-earth deformation and geoid changes due to large-scale mass redistribution processes. Observations of sea and land level changes from tide gauges and GPS are compared to the cumulative effect of GIA, present-day mass redistribution, and ocean dynamics over a 50 year period (1965–2014). GIA explains the majority of the observed sea-level and land motion trends, as well as almost all interstation variability. Present-day mass redistribution resulting from ice melt and land hydrology causes both land uplift and sea-level rise in the region. We find a strong correlation between decadal steric variability in the Subpolar Gyre and coastal sea level, which is likely caused by variability in the Labrador Sea that is propagated southward. The steric signal explains the majority of the observed decadal sea-level variability and shows an upward trend and a significant acceleration, which are also found along the coast. The sum of all contributors explains the observed trends in both sea-level rise and vertical land motion in the region, as well as the decadal variability. The sum of contributors also explains the observed acceleration within confidence intervals. The sea-level acceleration coincides with an accelerating density decrease at high latitudes.

1. Introduction

Observations show that sea level along the northwestern coast of the Atlantic Ocean north of Cape Hatteras (35°N, Figure 1) rises faster than the global average [*Boon*, 2012] and shows an acceleration over the last decades [*Ezer and Corlett*, 2012; *Sallenger et al.*, 2012]. However, the multitude of processes that affects regional sea level shows variability on a wide range of temporal scales, which hinders the separation between secular trends and accelerations and internal variability [*Haigh et al.*, 2014]. *Kopp* [2013] argues that in this region, the acceleration does not yet exceed the likely range of natural variability. Further insight can be obtained by considering the contribution of each individual process on regional sea level.

It is well-known that in general, regional sea level is influenced by multiple processes [*Stammer et al.*, 2013]. Along our region of interest, which covers the Atlantic coast between 35°N and 45°N, many studies discuss the individual contributors to sea-level trends, accelerations, and variability [e.g., *Bingham and Hughes*, 2009; *Engelhart et al.*, 2009; *Ezer*, 2013; *Woodworth et al.*, 2014; *Karegar et al.*, 2016], although to date, no study has yet combined these processes to close the regional sea-level budget.

Tide gauges are the main source of sea-level data over the last century, and the northwestern Atlantic coast is covered by a dense network of high-quality tide gauges with long records [*Woodworth et al.*, 2014]. Since tide gauges observe sea level relative to the land, tide gauges register vertical land motion (VLM) as a change in sea level. Permanent GPS receivers colocated with tide gauges can provide VLM rates, which allow separating vertical land motion from geocentric sea-level change [*Santamaría-Gómez et al.*, 2012; *Wöppelmann and Marcos*, 2016]. At many locations along the northwestern Atlantic coast, vertical land motion (VLM) forms a large contribution to sea-level changes [*Han et al.*, 2014]. The region is closely located to both the former Laurentide Ice Sheet and its forebulge location, and therefore large trends and regional differences in VLM, and thus in sea level, can be expected [*Engelhart et al.*, 2009; *Peltier et al.*, 2015]. Some stations in the region also suffer from local subsidence due to present-day groundwater depletion [*Karegar et al.*, 2016], while larger areas are affected by elastic uplift as a response to the decrease of surface load due to groundwater pumping [*Veit and Conrad*, 2016].

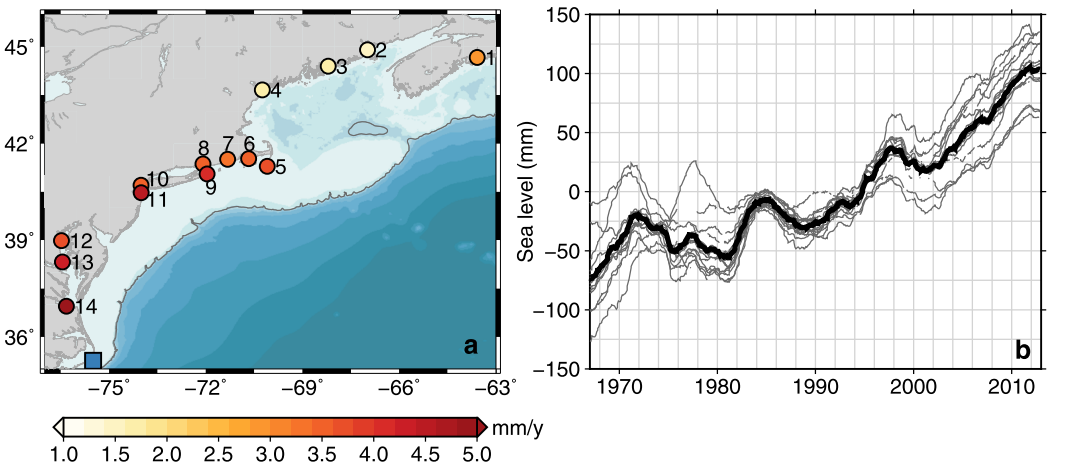

Figure 1. (a) Location of each tide gauge listed in Table 1. The color denotes the observed linear sea-level trend over 1965–2014 at the tide gauge, the gray line denotes the 250 m isobath, and the blue square denotes Cape Hatteras. (b) Residual time series of station-averaged sea level (thick, black) and each individual station (gray) after applying the regression model. The time series have been low-pass filtered using a 49 month running mean.

Next to GIA, present-day mass redistribution due to ice melt, land hydrology, and dam retention causes changes in global mean sea level (barystatic changes), as well as in regional relative sea level and vertical land motion [*Bamber and Riva*, 2010; *Santamaría-Gómez and Mémin*, 2015].

Multiple studies investigate the impact of processes related to atmosphere and ocean dynamics on sea level in this region. On decadal and multidecadal time scales, weakening of the Atlantic Meridional Overturning Circulation (AMOC) will cause a rise of the dynamic sea level along the coast [*Landerer et al*., 2007; *Bingham and Hughes*, 2009; *Ezer*, 2013]. Since the AMOC has only been observed directly since 2004, no information about its behavior is available on multidecadal time scales. Furthermore, *Thompson and Mitchum* [2014] argue that sea-level variability along the east coast of the North American continent has a common mode, caused by zonal transport between the ocean interior and the western ocean boundary. Next to large-scale oceanic forcing, regional wind forcing and the inverted barometer effect cause interannual variability of coastal sea level which may hide the effects of large-scale ocean dynamics on coastal sea level [*Woodworth et al*., 2014; *Li et al*., 2014; *Piecuch and Ponte*, 2015; *Piecuch et al*., 2016]. Hence, the effect of ocean dynamics consists of processes related to regional atmospheric forcing, and processes acting on larger spatial scales.

In this paper we investigate the influence of various large-scale processes on sea-level rise and variability along the American Atlantic coastline north of Cape Hatteras over the period 1965–2014. Over this period, high-quality tide gauge observations are available, as well as in situ subsurface temperature and salinity profiles in the northwestern Atlantic ocean, which are used to study the effects of ocean dynamics and changes in seawater density on coastal sea level. We use a self-consistent framework, similar to *Frederikse et al*. [2016], which explicitly incorporates the effects of GIA and present-day mass redistribution on both sea-level changes and vertical land motion. Using this framework, we compare the observed changes in sea level and land level with the sum of the individual processes. We show that the sum of the processes explains the observed decadal variability, trend, and acceleration in sea level along the northwestern Atlantic coast.

This paper is structured as follows: in section 2, we introduce the observed sea-level trends and variability from tide gauges and the linear rates of vertical land motion from GPS observations. In section 3 we discuss the role of GIA and introduce an updated data-driven model, which explains a large fraction of the observed VLM trends and most of the interstation variability. In section 4 the role of present-day mass transport due to ice melt and land hydrology is discussed. We show that present-day mass redistribution affects both sea-level and land-level observations and that the resulting VLM trends over the GPS era are not fully representative for the full 50 year study period. In section 5, we discuss the role of ocean dynamics on sea level in the region and show that steric changes in the Subpolar Gyre are highly correlated with sea-level changes

Table 1. List of Tide Gauge Stations Used in This Study, the Location, and the Accompanying GPS Station

Index	Name	Longitude	Latitude	GPS Station
1	Halifax	−63.58	44.67	HLFX
2	Eastport	−66.98	44.90	EPRT
3	Bar Harbor	−68.21	44.39	BARH
4	Portland	−70.25	43.66	YMTS
5	Nantucket Island	−70.10	41.29	IMTS
6	Woods Hole (Ocean. inst.)	−70.68	41.52	AMTS
7	Newport	−71.33	41.51	NPRI
8	New London	−72.09	41.36	CTGR
9	Montauk	−71.96	41.05	MNP1
10	New York (The Battery)	−74.01	40.70	NYBP
11	Sandy Hook	−74.00	40.46	SHK1, SHK2, SHK5, SHK6
12	Annapolis (Naval Academy)	−76.48	38.98	USNA
13	Solomon's Island (Biol. lab.)	−76.45	38.32	SOL1, MDSI
14	Sewells Point, Hampton Roads	−76.33	36.95	DRV1

along the coast. In section 6, we combine the estimates of all terms and present the estimate of the sea-level and VLM budget in the region and we show that the vast majority of the observed decadal variability, trend, and acceleration of sea level in the region can be explained by the individual processes. Finally, the discussion of the results and the conclusions are presented in section 7.

2. Sea-Level and GPS Observations

For the observations of trends and variability in mean sea level, we have selected 14 tide gauges from the Permanent Service for Mean Sea Level (PSMSL) database [*Holgate et al*., 2013]. We have selected stations that are within 25 km of one or more permanent GPS stations and are not known for datum instability. All tide gauge stations with their location and GPS stations are listed in Table 1. Local barotropic effects may play a large role in the variability at individual tide gauge locations. Since we are interested in a region-mean signal, we remove the local effects of the seasonal cycle, wind stress, and sea-level pressure from monthly mean sea level by applying a simple linear regression model, similar to the procedure followed in *Dangendorf et al*. [2014a]. Indices of wind and sea-level pressure have been obtained from the twentieth Century Reanalysis project version V2C [*Compo et al*., 2011]. For each index we select the grid cell within a 250 km radius of the tide gauge with the highest correlation with monthly mean sea level. We subsequently estimate the least squares coefficients and the confidence intervals using linear least squares,

$$\begin{aligned}\zeta(t)=\zeta_0+\alpha_1 t+\frac{1}{2}\alpha_2 t^2+\alpha_3(p(t)-\bar{p}(t))+\alpha_4\tau_u(t)+\alpha_5\tau_v(t)\\ +\beta_1\ \sin\left(\frac{2\pi t}{365.25}\right)+\beta_2\ \cos\left(\frac{2\pi t}{365.25}\right)+\beta_3\ \sin\left(\frac{2\pi t}{182.63}\right)+\beta_4\ \cos\left(\frac{2\pi t}{182.63}\right),\end{aligned} \tag{1}$$

with $\zeta(t)$ monthly mean sea level, ζ_0 mean sea level, t the time epoch, $p(t)$ sea-level pressure, $\bar{p}(t)$ sea-level pressure averaged over all oceans, and τ_u and τ_v the zonal and meridional wind stress. When the estimated values of α_3, α_4, and α_5 are significant (i.e., their 95% confidence interval does not cross zero), their accompanying regressor is removed from the mean sea-level time series, as well as the mean ζ_0 and the annual and semiannual cycle $(\beta_1, \beta_2, \beta_3, \beta_4)$. The linear trend and acceleration term are coestimated, but not removed from the signal. Note that leaving out the trend or acceleration estimate in equation (1) has a negligible effect on the resulting regression coefficients. Supporting information Figure S1 shows the signal that is removed for each individual station, as well as the station-mean removed and retained signals. Consistent with findings of *Piecuch and Ponte* [2015] and *Woodworth et al*. [2014], the removed signal also contains a station-mean signal, although this signal is smaller than the residual station-mean signal and does not show a significant trend or acceleration. Also for the individual stations, the removed signal does not contain significant trends or accelerations.

To test the sensitivity of the regression model against the choice of the reanalysis product, we have tested our regression model using data from the JRA55 reanalysis [*Kobayashi et al*., 2015] and the ICOADS 3.0 gridded observations database [*Freeman et al*., 2016]. Both data sets cover the full 1965–2014 period. The removed and retained signals for these data sets are also shown in supporting information Figure S1.

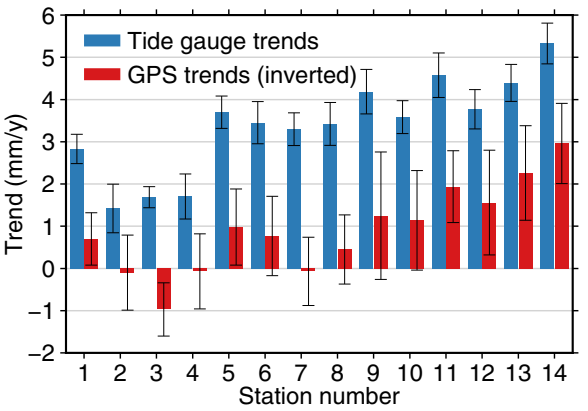

Figure 2. Linear trends and confidence intervals in observed vertical land motion (red) and relative sea level (blue) at each tide gauge site. Note that the trends in vertical land motion have been inverted.

Choosing a different model does not have a large effect on the resulting station-mean variability signal. However, the removed signal using JRA55 and ICOADS does have a significant linear trend, while the twentieth Century Reanalysis does not. To account for this uncertainty, we use the standard deviation of the different trends as a source of uncertainty. The removed signal does not contain a significant acceleration, regardless of the data set used.

After the removal of the local effects of wind and air pressure, the linear trends and accelerations, together with their uncertainties, are estimated for each time series by assuming a generalized Gauss-Markov (GGM) noise structure. This noise model adequately describes the serially correlated noise structure in most tide gauge time series [*Bos et al.*, 2014]. The Hector software [*Bos et al.*, 2013] is used to compute the trends, accelerations, and their uncertainties. The uncertainty related to the use of different models for the regression analysis is added in quadrature to the error estimates. All confidence intervals presented in this study are at the one sigma level.

To separate decadal variability from high-frequency signals, the time series, after correcting for wind and pressure, are low-pass filtered using a 49 month running mean. Note that trends and accelerations are estimated from the signal before the running mean filter is applied.

The station locations and the observed linear trends are depicted in Figure 1a. The linear trends show large interstation differences, with lower trends mostly located in the northeast and higher trends in the southwest. On the other hand, the pattern of decadal variability after applying the regression model, shown in Figure 1b, is very similar between stations. This coherent pattern of decadal variability has already been observed in many studies [e.g., *Thompson*, 1986; *Thompson and Mitchum*, 2014; *Woodworth et al.*, 2014].

For each GPS receiver, linear vertical land motion trends have been obtained from the Nevada Geodetic Laboratory (geodesy.unr.edu). For some tide gauge stations, multiple GPS receivers are nearby. In that case, the rates of all nearby GPS stations have been averaged. The provided trends have been computed using the MIDAS robust trend estimator [*Blewitt et al.*, 2016], which provides trends and uncertainties that are not affected by unknown jumps in GPS time series, which could cause large biases if they remain uncorrected [*Gazeaux et al.*, 2013]. The vertical land motion rates as observed by GPS and their confidence intervals are depicted in Figure 2. The rates have been inverted and plotted next to the observed sea-level trends. A clear connection between the sea-level and inverted land-motion trend can be seen: stations with high sea-level trends generally show high subsidence and vice versa. The distinct northeast-southwest pattern of lower and higher rates in the tide gauge records can also be observed from GPS. The difference between the observed sea-level and inverted VLM trend does not show large variations over the region, which suggests that the large interstation differences have their origin mostly in vertical land motion. In the next sections we will examine the influence of glacial isostatic adjustment (GIA) and present-day mass transport on the regional sea-level and VLM trends and whether these processes explain the differences between the individual stations.

3. Glacial Isostatic Adjustment

The primary candidate for explaining the differences between the individual stations in observed sea-level and land-level change is glacial isostatic adjustment (GIA). GIA affects both GPS and tide gauge observations: deformation of the solid earth is registered as vertical land motion by GPS observations, while tide gauges observe changes in relative sea level, which is a combination of solid-earth deformation, geoid changes, and a global-mean eustatic term that ensures conservation of mass [*Tamisiea*, 2011].

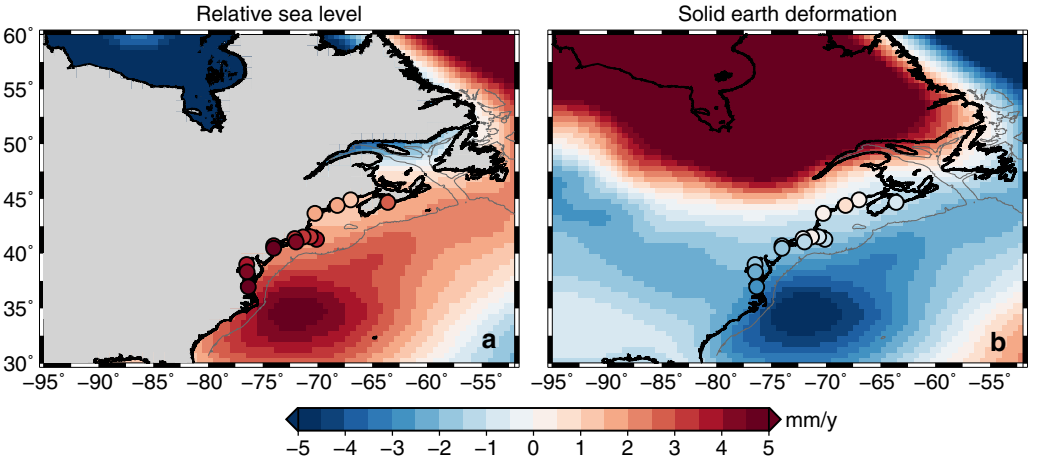

Figure 3. Modeled present-day trend in (a) relative sea level and (b) land level due to glacial isostatic adjustment. Tide gauge locations are marked by dots, with the color of the dot denoting (a) observed relative sea-level trend and (b) observed vertical land motion trend.

The observed northeast-southwest gradient in relative sea level has already been linked to GIA in multiple studies [*Engelhart et al*., 2009; *Kopp*, 2013]. Both uplift due to the proximity of the former Laurentide Ice Sheet, and subsidence caused by the collapse of the ice sheet forebulge occur in our region. Both effects result in a complex uplift-subsidence structure that poses a challenge for many GIA models [*Davis and Mitrovica*, 1996; *Roy and Peltier*, 2015]. Here we revisit the influence of GIA in the region with the regional GIA model from *Simon and Riva* [2016]. This model is based on a joint inversion of VLM rates from GPS, gravity rates from GRACE, and a large suite of forward GIA models that spans plausible ice sheet and earth viscosity model parameters. Compared to the global ICE6G-VM5a model [*Peltier et al*., 2015], the resulting GIA solution gives an overall lower misfit to observed gravity changes and vertical land motion over the North American continent [*Simon and Riva*, 2016]. In addition to most GIA models, this model also provides estimates of the formal uncertainty of the predicted sea-level and land-level velocities. Supporting information Figure S2 shows a comparison between the GIA model employed here and the global ICE6G-VM5a model [*Peltier et al*., 2015].

The modeled present-day trends in sea level and land level caused by GIA, together with the observed trends in sea level and land level, are shown in Figure 3. The location of the forebulge collapse is visible as a positive trend in relative sea level (Figure 3a) and strong land subsidence (Figure 3b). The predicted region of the forebulge collapse coincides well with the southwestern stations that show high rates of subsidence and sea-level rise. The northeastern stations are located farther away from the middle of the forebulge collapse area, and relative to the more southerly stations, are characterized by less negative or slightly positive rates of VLM. Therefore, the horizontal gradient in observed vertical land motion and sea-level rise along the coastline, as shown in Figure 2a, is consistent with the complex structure seen in the predicted present-day effect resulting from GIA. When the relative sea-level estimates are removed from the tide gauge observations, the interstation spread, visible in Figure 1b, is reduced, as depicted in Figure 4. The standard deviation of the observed relative sea-level trends is reduced from 1.12 mm/yr without GIA correction to 0.66 mm/yr after removing the local GIA signal.

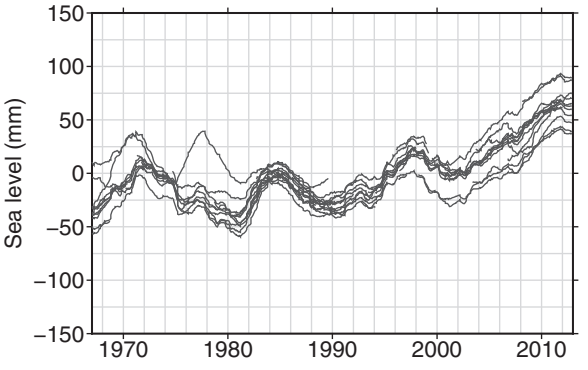

Figure 4. Time series of the individual tide gauge records after removing the modeled relative sea-level response to GIA. The time series have been low-pass filtered using a 49 month running mean.

However, it must be noted that the exact location of the forebulge is uncertain and the presence of a strong gradient in modeled vertical land motion and sea-level

trends perpendicular to the coastline makes sampling of the GIA signal at tide gauge stations prone to errors, which are not fully quantified in the formal uncertainty estimates.

4. Present-Day Mass Redistribution

Redistribution of mass between land and ocean causes, in addition to changes in the global-mean barystatic sea level, regionally varying sea-level changes. These regional variations are caused by changes in the earth gravity field (geoid changes), deformation of the solid earth, and earth rotation effects [*Tamisiea and Mitrovica*, 2011]. Hence, similar to GIA, both tide gauge and GPS observations are affected by present-day mass redistribution. In this section, we quantify the influence of the major mass exchange processes on sea level and vertical land motion in our region of interest.

The effects of mass redistribution on sea level are computed by solving the elastic sea-level equation [*Farrell and Clark*, 1976]. We apply the spherically symmetric approximation and solve the equation in the center-of-mass (CM) frame using the pseudo-spectral method as described by *Tamisiea et al*. [2010]. The earth rotation effect is modeled following the description in *Sabadini et al*. [2016]. The resulting effects of mass transport on local observations of relative sea level can be split in different contributors,

$$\eta'(\theta,\phi,t)=\bar{\eta}'(t)+G'(\theta,\phi,t)-R'(\theta,\phi,t), \tag{2}$$

$\eta'(\theta,\phi,t)$ is the local relative sea-level anomaly at longitude ϕ and latitude θ and time t as a result of the mass redistribution, which is observed by tide gauges. $\bar{\eta}'(t)$ is the global-mean term that is required to ensure global mass conservation. $G'(\theta,\phi,t)$ denotes changes of the geoid and $R'(\theta,\phi,t)$ is the resulting deformation of the solid earth. Note that $\bar{\eta}'(t)$ is not the same as the global-mean barystatic contribution, since the geoid and solid earth deformation fields do not evaluate to zero over the whole ocean. Mass redistribution affects GPS observations only by the resulting solid earth deformation, while tide gauge observations are affected by all processes on the right-hand side of equation (2).

Here we consider the large-scale mass redistribution due to glacier and ice sheet melt, natural hydrology, groundwater depletion, dam retention, and the 18.6 year nodal tide. Except for the Greenland ice sheet, we use the same estimates for the individual mass redistribution processes as in *Frederikse et al*. [2016], which provides a detailed description of the used models and the derivation of formal uncertainties. Here we review the mass redistribution models briefly. For glacier melt, we use the modeled mass balance estimates of *Marzeion et al*. [2015], which provides estimates of the mass evolution of 18 glacierized regions.

For the Greenland Ice Sheet, the mass balance estimates and their uncertainties from *Kjeldsen et al*. [2015] are used before 1992. After 1992, the Greenland mass change is estimated from the Surface Mass Balance (SMB) and solid ice discharge. SMB is modeled using RACMO2.3 [*Noël et al*., 2015], while ice discharge is modeled using a constant acceleration of 6.6 Gigaton/yr^2, based on results from *van den Broeke et al*. [2016]. For the Antarctic ice sheet, we assume no mass changes before 1979, a long-term balance between the Antarctic Ice Sheet SMB [*van Wessem et al*., 2014] and ice discharge between 1979 and 1992, and we assume 2.0 Gt/yr^2 acceleration of the ice discharge after 1993, which gives a reasonable fit to both the results of the IMBIE intercomparison case [*Shepherd et al*., 2012] and GRACE observations of ice mass loss over more recent years [e.g., *Watkins et al*., 2015]. Note that the contribution of the Antarctic ice sheet before the nineties is very uncertain, although observations of earth rotation suggests that the total ice sheet contribution before the nineties is probably below 0.2 mm/yr [*Mitrovica et al*., 2015].

The resulting regional sea-level patterns are sensitive to the location of mass loss. Therefore, the mass loss of each ice sheet is partitioned by scaling the ice-sheet averaged trend by the individual trend in each grid cell, computed from GRACE mascon solutions [*Watkins et al*., 2015]. Variability in natural hydrology and the depletion of groundwater are based on the outcomes of the PCR-GLOBWBv2 global land hydrology model [*Wada et al*., 2011, 2014]. For dam retention, we have used the GRanD Global Reservoir and Dam database [*Lehner et al*., 2011] to estimate the location and capacity of all reservoirs. The filling and seepage rates of the reservoirs are estimated following the method of *Chao et al*. [2008]. The astronomical nodal cycle causes a tidal signal with a period of 18.61 years. This tidal signal also acts as a mass redistribution process, and thus results in geoid changes and solid earth deformation. We model the effects of the nodal cycle under

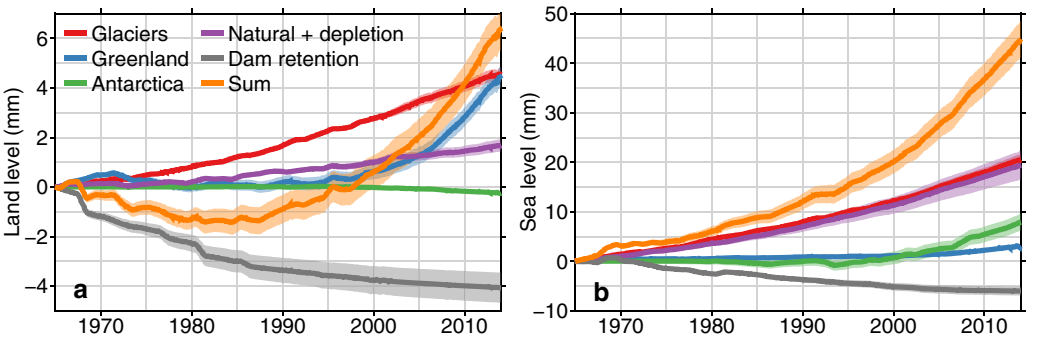

Figure 5. Station-mean effects of the individual mass transport terms and their sum: (a) resulting vertical land motion and (b) relative sea level. The shading denotes the uncertainty at 1σ.

the assumption that the amplitude and phase of the nodal cycle do not depart from tidal equilibrium [*Woodworth*, 2012]. Since our region is close to 35° latitude, where the amplitude of the nodal cycle is zero, the impact of the nodal cycle is small, with an amplitude of about 1–4 mm in sea level and 0–0.2 mm in the solid earth height.

For each individual process, the sea-level equation is solved for the annual-mean mass redistribution. The time series of vertical land motion and sea-level change resulting from the individual mass transport processes and their confidence intervals, averaged over all 14 stations, are depicted in Figure 5. The resulting vertical land motion from the sum of processes shows a clear acceleration. Mostly due to the decrease in dam construction and the increase of Greenland melt, the solid earth response shows an upward acceleration since the nineties (Figure 5a). Note that due to its proximity, Greenland mass loss causes uplift in the region, while the distant Antarctic ice sheet causes subsidence. Due to the acceleration since the nineties, the region-mean VLM trend since 2000 is in the order of 0.5 mm/yr. This trend is larger than the trend over the full period, which is in the order of 0.1 mm/yr. Since GPS observations typically cover only the last 10–15 years, the observed trend over that period is not fully representative for the long-term VLM trend. This difference causes a bias if the GPS trend is assumed to be representative for the full tide gauge record.

Even though the land motion caused by the present-day mass contributors is positive, the cumulative effect of all contributors still results in a positive relative sea-level trend and an acceleration over the period of interest.

Since the northernmost station Halifax and the southernmost station Sewells Point are about 1500 km apart and the region is in close proximity to some glacierized regions and the Greenland ice sheet, interstation differences in the mass contribution to sea-level rise are present. In Figure 6 these differences are quantified by estimating the linear trend resulting from each contributor and their sum at each grid cell. A gradient along the coast can be seen in the contribution of glaciers and Greenland (Figures 6a and 6b), while the other processes (Figures 6c–6e) vary less over the region. The sum of processes (Figure 6f) shows that in our region of interest the interstation differences are in the order of 0.1 mm/yr, which is an order of magnitude smaller than the differences caused by GIA. Therefore, present-day mass transport will only explain a negligible fraction of the observed interstation variability in sea-level trends.

5. Ocean Dynamics

We have now quantified the major past and present-day mass transport effects, and the next step is to determine the role of ocean dynamics on coastal sea level. Since we have applied a simple regression model (equation (1)) to remove the local impact of wind and pressure, we will look for remote drivers of variability. Due to the presence of, among other processes, boundary waves and currents, coastal sea-level trends, and variability are often decoupled from the nearby open ocean, even on decadal time scales [*Bingham and Hughes*, 2012]. In contrast, coastal sea level often shows alongshore coherence over thousands of kilometers [*Hughes and Meredith*, 2006]. Hence, we cannot directly use the steric height signal in the nearby open ocean as a proxy for dynamic sea-level changes along the coast. To determine whether a link exists between dynamic sea-level changes in the open ocean and along the coast, we determine the correlation

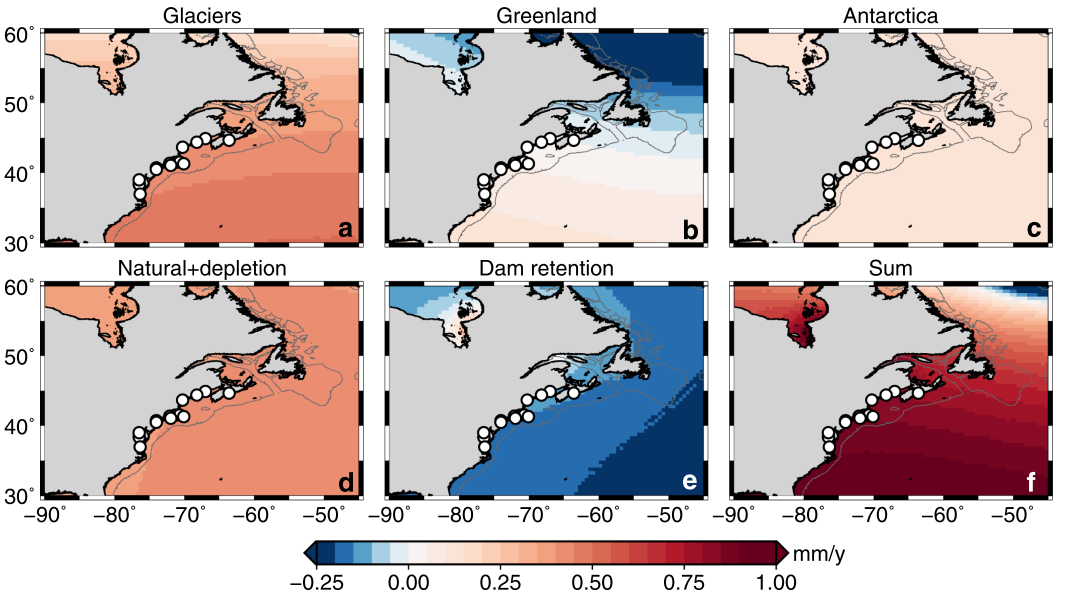

Figure 6. Linear trends in the resulting relative sea-level changes caused by (a–e) each individual present-day mass redistribution process and (f) the sum of these processes.

between tide gauge and altimetry observations. We obtained a multimission gridded altimetry sea-level anomalies product from Archiving, Validation and Interpretation of Satellite Oceanographic data (AVISO). A Gaussian filter with a half-width of 75 km has been applied to the fields to remove high-frequency signals related to ocean eddies. The correlation pattern between region-mean sea level from tide gauges and sea level in the Northwest Atlantic from altimetry is shown in Figure 7a. This figure clearly shows a high correlation over the shelf along the coast, which confirms that the coastal sea-level signal is reproduced by altimetry. Furthermore, a large area of high correlation is visible in the southern part of the North Atlantic Subpolar Gyre. Both findings correspond well to the results of *Andres et al*. [2013], who also found this correlation pattern. If we remove the signals related to present-day mass effects from the tide gauge and altimetry records, and we recompute the correlation (Figure 7b), coastal sea level is also highly correlated with the boundary of the North Atlantic Ocean along the coast of Greenland. One of the main reasons for the improvement in the correlation pattern after removing the mass contributors is the contribution of the 18.6 year nodal cycle. Its amplitude increases with higher latitudes and forms a substantial contribution to the decadal sea-level signal around Greenland. Removing the equilibrium nodal cycle from the altimetry record

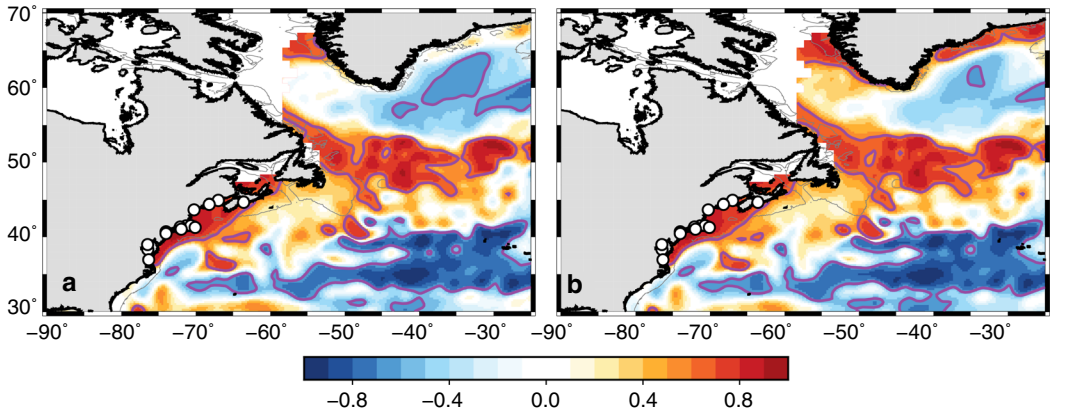

Figure 7. Correlation of region-mean sea level from tide gauges and altimetry sea level at each grid cell. (a) Correlation between the original tide gauge and altimetry signals. (b) Correlation after removing the effects of present-day mass transport from both tide gauge and altimetry data. All time series have been detrended and low-pass filtered using a 49 month running mean before computing the correlation. The gray line depicts the 250 m isobath and the white circles show the tide gauge locations. The purple line encircles the areas for which the correlation is significant at the 95% level.

explains the majority of the observed increase in correlation along the Greenland coast. Because we have removed all mass signals, this correlation pattern must have its origin in ocean dynamics. Hence, this correlation pattern suggests a link between sea-level variability in the boundary current of the Subpolar Gyre and dynamic sea level near the coast.

Since density effects are one of the factors that drive dynamic sea-level changes, the next step is to use in situ temperature and salinity observations to compute steric height changes. Regular in situ measurement campaigns have been conducted in the region [*Kieke and Yashayaev*, 2015], which allows us to estimate steric height changes over the last 50 years from in situ data. However, in the northern part of the Subpolar Gyre, the amount of observations is lower, and due to sea ice and weather conditions, biased toward summer observations. We computed steric heights from the EN4 data set (*Good et al*. [2013], version 4.1.1, with the *Gouretski and Reseghetti* [2010] XBT and MBT fall rate correction applied.) over the period 1965–2014. The EN4 database provides gridded temperature and salinity observations, from which steric height anomalies are derived using the TEOS-10 package [*Roquet et al*., 2015]. Since the amount of observations below 2000 m in the Subpolar Gyre is limited, we only use observations in the upper 2000 m. We computed the correlation between the station-mean tide gauge signal, with the mass signal removed, and steric height anomalies, evaluated over the upper 2000 m. The correlation pattern (Figure 8a) shows that the high correlation between coastal sea-level changes and dynamic sea-level changes in the southern part of the Subpolar Gyre in Figure 7b is also visible in in situ observations over a longer time span. Since steric height changes in shallow water are small, the correlation between on-shelf steric height and tide gauge observations decreases, which probably causes the low correlation on the shelf in Figure 8a.

The observed high correlation between dynamic sea level on the shelf and in the southern Subpolar Gyre is in line with multiple modeling studies. *Häkkinen* [2001] finds a coherent decadal sea-level signal in the Subpolar Gyre and along the US east coast using empirical orthogonal functions from model data. Using highly simplified models, *Hsieh and Bryan* [1996] and *Johnson and Marshall* [2002] argue that Kelvin waves along the western boundary of the North Atlantic result in a quick alongshore adjustment to sea-level perturbations at high latitudes. This quick response is followed by a slower response resulting from advective processes. However, the sidewalls of the western boundary are not vertical, and hence the boundary wave propagation will take the form of a coastally trapped wave instead of a pure Kelvin wave [*Huthnance*, 1978]. Using an isopycnal ocean model with realistic topography, *Roussenov et al*. [2008] find that sea surface height anomalies in the Labrador Sea propagate along the southern Subpolar Gyre and the western boundary of the North Atlantic coast. *Hodson and Sutton* [2012] confirm this propagation mechanism and argue that the propagated density anomalies at 800–1800 m depth are related to changes in the AMOC strength. *Roberts et al*. [2013] compare multiple coupled climate models, and using a lead-lag correlation analysis, they show that density anomalies in the Labrador Sea are propagated both along the Subpolar Gyre and the western boundary. Hence, these model results clearly suggest that the correlation pattern in Figure 8 is

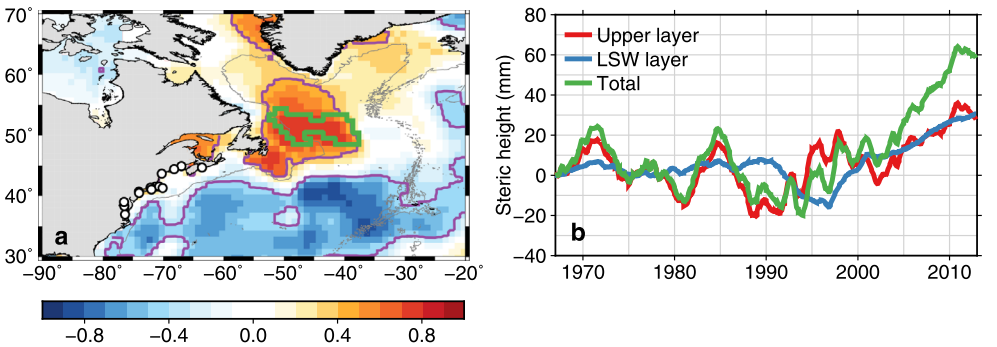

Figure 8. Observed steric height signal. (a) Correlation between observed tide gauge sea level over 1965–2014 after present-day mass effects have been removed and steric height integrated from the surface to either the ocean floor or 2000 m, depending on which is reached first. The gray line depicts the 2000 m isobath. All time series have been detrended and low-pass filtered using a 49 month running mean before computing the correlation. The purple line encircles the areas for which the correlation is significant at the 95% level. (b) Time series of steric height over the upper layer (0–650 m), the LSW layer (650–2000 m) and the full layer averaged over the area encircled by the green line in Figure 8a.

a result of high-latitude anomalies that are propagated both into the Subpolar Gyre and along the western boundary. These adjustment processes not only result in a coherent sea-level variability signal, but on multidecadal time scales, also on a coherent sea-level rise signal [*Yin et al*., 2009].

To obtain a proxy for the high-latitude sea-level anomalies that affect coastal sea level, we average the steric signal over the region of high correlation in the southern Subpolar Gyre. We define this region as all grid cells with a depth of at least 2000 m, a positive correlation coefficient and a positive coefficient of determination (R^2) with detrended coastal sea level. These points are encircled by the green line in Figure 8a. The resulting time series of steric height changes in the area encircled by the green line is shown in Figure 8b. The steric signal is not correlated with the signal that has been removed by the regression analysis in equation (1) (correlation coefficient of 0.06 between both low-pass filtered and detrended signals).

Various processes may be responsible for the observed steric variations. In the upper ocean, the East and West Greenland Current and the Labrador Current form a cyclonic boundary current system [*Fischer et al*., 2004]. The variability in this upper layer is largely driven by atmospheric processes [*Han et al*., 2010]. At intermediate depths, Labrador Sea Water (LSW) can be found, which is formed during deep convection events in the Labrador Sea. After formation, LSW is transported at depth along the western boundary of the Atlantic by the Deep Western Boundary Current [*Rhein et al*., 2011]. This DWBC forms the lower limb of the Atlantic Meridional Overturning Circulation (AMOC), and changes in the density of LSW are believed to impact its strength [*Robson et al*., 2014]. Model predictions show that changes in the AMOC strength have a large impact on sea level along the US coast, and its projected slowdown in a warmer climate leads to sea-level rise in the Subpolar Gyre and along the US coast [*Yin et al*., 2009; *Bingham and Hughes*, 2009]. Below the LSW deep water masses are present that are formed from Denmark Strait Overflow Water (DSOW) and Iceland-Scotland Overflow Water (ISOW), which are also transported by the DWBC [*Rhein et al*., 2011].

To separate the signal of these different water masses on our proxy for the high-latitude steric variability, we compute the steric height variability over the depth layers that contain these different water masses. These layers can be separated using a potential density anomaly criterion. Following *Rhein et al*. [2011], we define Labrador Sea Water as water with a potential density anomaly of $\sigma_\theta = [27.68, 27.80]\ \mathrm{kg/m^3}$. When we average the potential density anomalies over the area of high correlation (denoted by the green line in Figure 8a), we find LSW below 650 m depth. The lower bound of the LSW layer is generally located around or below 2000 m (see supporting information Figure S3). The resulting steric height anomalies in both layers and over the full column, averaged over the area of high correlation, are depicted in Figure 8b. The upper layer (red line) exhibits strong decadal variability, while variability in the deeper layer (blue line) acts mostly on multidecadal scales with an acceleration starting halfway into the nineties. Due to the limited availability of observations below 2000 m, we do not include the effects of changes in deep water density on coastal sea level. The steric signal integrated over both layers (green line) contains a strong increase in steric height since the nineties.

In this section, we have shown that a strong correlation exists between steric variability on decadal scales along the northwestern Atlantic coast and in the Subpolar Gyre. Multiple model studies pointed at a very similar correlation pattern, which is related to the southward propagation of density anomalies in the Labrador Sea. We use the density changes in the southern Subpolar Gyre as a proxy for the impact of this high-latitude variability on the trend and decadal variability of coastal dynamic sea level. Therefore, we use the steric signal in the upper 2000 m in the southern Subpolar Gyre (denoted with the green line in Figure 8b) as a proxy for dynamic sea-level response along the northwestern Atlantic coast to this variability.

6. Regional Vertical Land Motion and Sea-Level Budgets

In the previous sections, we have obtained estimates of the impact of GIA, present-day mass transport, and high-latitude steric variability on coastal sea-level changes. In this section we compare the sum of all contributors with the observed sea level and vertical land motion and verify whether the regional sea-level budget can be closed between 1965 and 2014. To avoid the bias due to nonlinear solid earth deformation resulting from present-day mass redistribution, we split the observed VLM trends into two known contributors and the residual trend,

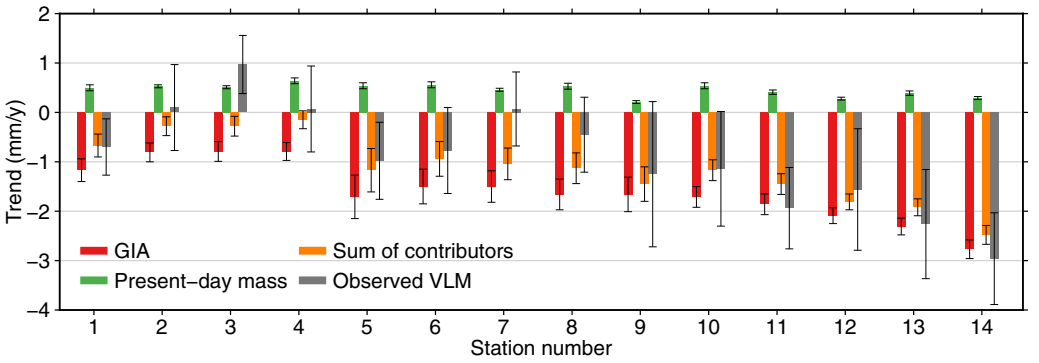

Figure 9. Modeled and observed vertical land motion at each tide gauge, together with the uncertainty estimate on the 1σ level. The trends of solid-earth deformation resulting from present-day mass redistribution are computed over the time span of the individual GPS record. The sum of contributors consists of the effects of solid earth deformation due to GIA and present-day mass redistribution. The stations are numbered according to Table 1.

$$\frac{d\bar{z}}{dt} = \frac{d\bar{R}_{\mathrm{GIA}}}{dt} + \frac{d\bar{R}_{\mathrm{PD}}}{dt} + \frac{d\bar{z}_r}{dt}, \tag{3}$$

with $\frac{d\bar{z}}{dt}$ the observed linear VLM trend. $\frac{d\bar{R}_{\mathrm{GIA}}}{dt}$ is the modeled linear VLM trend resulting from GIA. $\frac{d\bar{R}_{\mathrm{PD}}}{dt}$ is the linear trend in solid earth deformation resulting from present-day mass redistribution over the period covered by the GPS observation at each station. $\frac{d\bar{z}_r}{dt}$ is the residual vertical land motion that cannot be explained by the other terms. We make the assumption that the residual VLM term stays constant over the complete time span, and the residual VLM term appears as a linear trend in the relative sea-level budget. The VLM budget for each GPS station is shown in Figure 9. For most stations, the largest fraction of the observed VLM trend can be explained by GIA, which varies considerably over the region. Present-day mass effects cause an uplift rate in the order of 0.5 mm/yr. The interstation differences in the contribution of present-day mass effects are largely caused by different lengths of the GPS records and only to a small extent by spatial variability of the solid earth deformation. For twelve out of fourteen stations, the combination of GIA and present-day mass effects explain the observed VLM trend within confidence intervals. For two stations (3 and 7), a significant difference between the modeled and observed VLM remains.

Now we have removed the impact of GIA and present-day mass redistribution on vertical land motion, we can use the modeled relative sea-level change from equation (2) in our budget. When we combine all terms, our sea-level budget equation reads,

$$\eta_{\mathrm{Sum}}(t) = \eta_{\mathrm{GIA}}(t) + \eta_{\mathrm{PD}}(t) + \eta_{\mathrm{Dyn}}(t) - \bar{z}_r(t). \tag{4}$$

Here $\eta_{\mathrm{Sum}}(t)$ is the sum of the modeled contributors. $\eta_{\mathrm{GIA}}(t)$, $\eta_{\mathrm{PD}}(t)$, and $\eta_{\mathrm{Dyn}}(t)$ are the contributions of GIA, present-day mass transport, and ocean dynamics. The ocean dynamic contribution is approximated by the open-ocean steric signal from the Northwest Atlantic, as discussed in section 5, and displayed in Figure 8b. For the ocean dynamics, similar to the observed sea level, we assume that the temporal autocorrelation of the noise follows a Generalized Gauss-Markov distribution. We use this budget equation to compute trends in all contributors and compare their sum with the observed trend in sea level. The budget for each individual station is depicted in Figure 10. For each individual station, the observed sea-level trend can be explained by the sum of contributors within the overlapping confidence interval. Again, GIA is the dominant term, especially for the southwestern stations. The role of present-day mass and ocean dynamics are both similar in size. Note that for each stations, the same proxy for ocean dynamics is used. Also for present-day mass effects, the interstation spread is small. The residual VLM term is generally smaller than the other terms, but for some stations, its size is considerable.

To obtain a region-mean budget, we average the observed and modeled time series of the individual stations. To obtain estimates for the station-mean uncertainties, we use the average uncertainty of all individual contributors, since these processes have a common origin. For the uncertainty in vertical land motion, we assume that the errors of the individual stations are independent, and the individual VLM uncertainty estimates are averaged in quadrature. The uncertainty of the observed station-mean sea level is computed

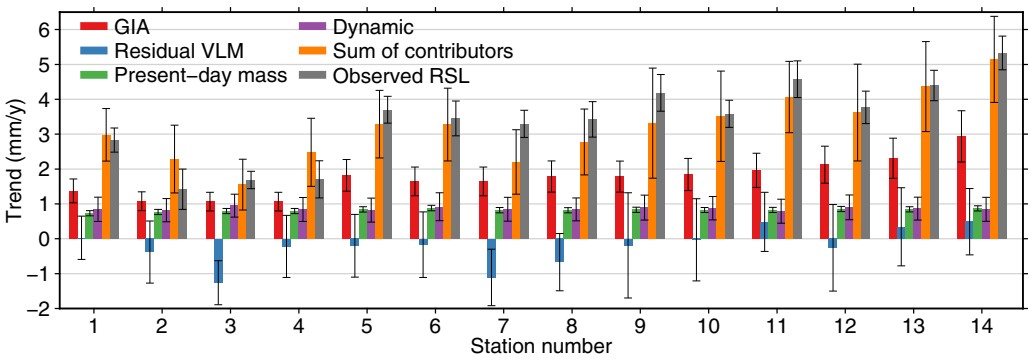

Figure 10. Observed and modeled trends (1965–2014) in sea level for all individual stations, together with the accompanying uncertainty estimates. The residual VLM term is inverted to show its contribution to the sea-level budget.

under the assumption of a generalized Gauss-Markov (GGM) noise structure, with the uncertainty that originates from the regression model, as discussed in section 2, added in quadrature. The resulting region-mean trends and accelerations are listed in Table 2. As expected, GIA dominates the station-mean linear trend. The nodal cycle only plays a very small role, while the residual VLM term is not significantly different from zero. As for each individual station, the sum of contributors explains the observed station-mean trend well within the confidence intervals.

Under the assumption that the noise in the observations follows a generalized Gauss-Markov (GGM) distribution, the observed sea level shows a significant upward acceleration of 0.126 ± 0.046 mm/yr^2 over our period of interest. The acceleration in present-day mass redistribution is positive, but too small to explain the acceleration in observed sea level. The acceleration of the ocean dynamics term is larger than the mass redistribution term, and when both terms are added, the acceleration in observed sea level can be explained within confidence intervals. Hence, the observed large acceleration in regional sea level can be linked to the ocean dynamics signal.

To study the origin of the observed decadal sea-level variability, the observed station-mean sea-level time series and the individual contributors are shown in Figure 11a. The ocean dynamics term explains almost all observed decadal variability, while the contribution of present-day mass largely consists of an acceleration and does not show substantial decadal variability. GIA and residual VLM are assumed to be linear, and hence, only explain a part of the observed trend. When we compare the time series of observed sea level to the sum the individual contributors (Figure 11b), we see that both the long-term trend as well as the majority of observed decadal variability are explained by the sum of contributors: the correlation between the detrended observation and sum of contributors is 0.86, with a coefficient of determination (R^2) of 0.68. The residual is depicted in Figure 11c. The bound of the confidence interval, which is computed by summing the confidence intervals of the individual terms in quadrature, does not significantly deviate from zero, except for one distinctive event around 1997, where the peak in coastal sea level is not captured by the steric height observations. We have verified the altimetry observations, which do show a similar peak around 1997 in the Subpolar Gyre. Furthermore, the profiles show an unstable stratification in 1997 (see supporting information Figure S3), which suggests that the mismatch may be related to issues with the hydrographic profiles.

These results show that a large fraction of the observed sea-level acceleration

Table 2. Linear Trends and Accelerations for Individual Contributors, the Sum of Contributors and Observed Relative Sea Level Over 1965–2014[a]

	Linear Trend (mm/yr)	Acceleration (mm/yr^2)
Glaciers	0.41 ± 0.02	0.009±0.001
Greenland	0.04 ± 0.01	0.003±0.001
Antarctica	0.12 ± 0.03	0.015±0.002
Dam retention	−0.14±0.02	0.003 ± 0.001
Natural + depletion	0.40 ± 0.06	0.010 ± 0.003
Present-day mass	0.83 ± 0.07	0.040 ± 0.003
Ocean dynamics	0.88 ± 0.25	0.136 ± 0.038
GIA	1.75 ± 0.44	
−Residual VLM	−0.22±0.26	
Nodal cycle	−0.02±0.00	
Sum of contributors	3.22 ± 0.57	0.176 ± 0.038
Observed RSL	3.35 ± 0.38	0.126 ± 0.046

[a]The uncertainties are on the 1σ level. The bold contributors are summed to obtain the total contribution.

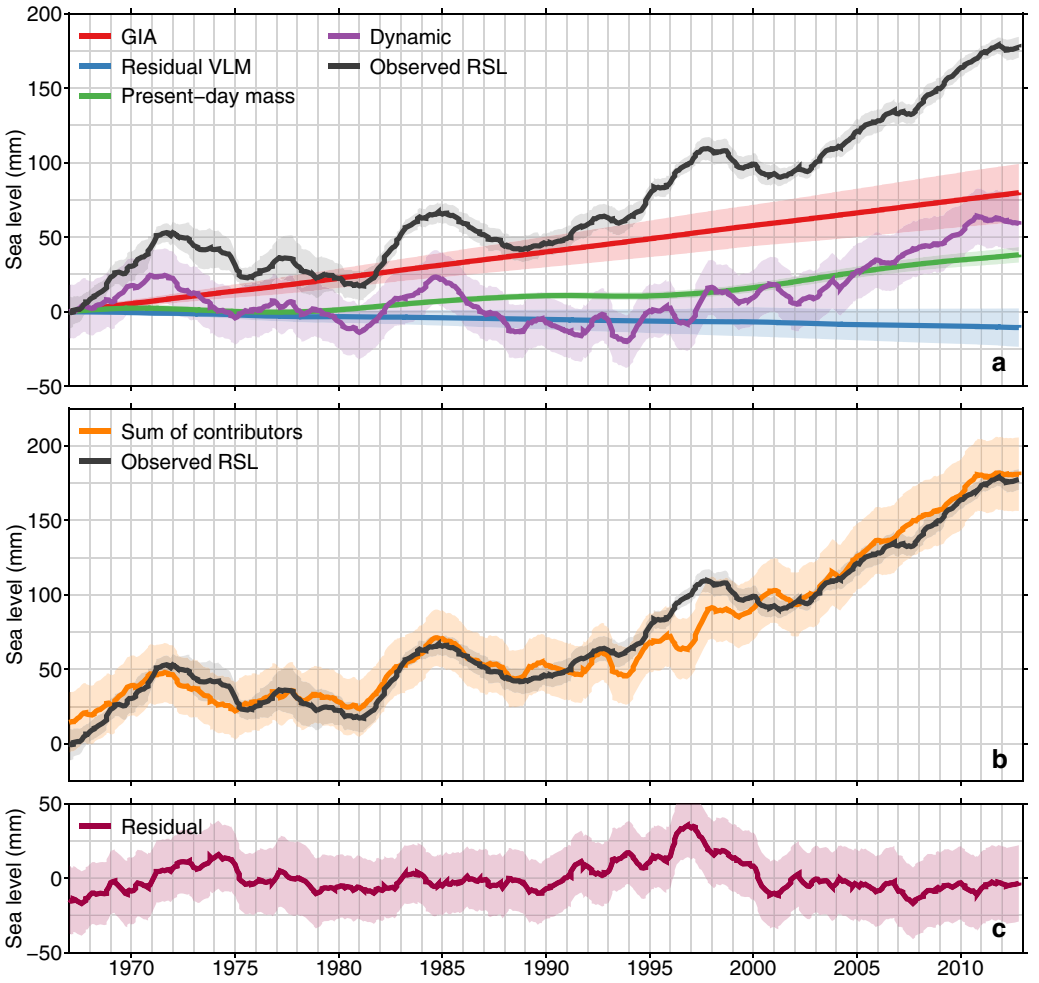

Figure 11. Region-mean sea-level budget. (a) Individual contributing processes and observed sea level. (b) Sum of all contributing processes. (c) Observations minus sum of contributors. Shaded areas denote the confidence interval of all processes at the one sigma level. All time series have been low-pass filtered with a 49 month running mean.

and decadal sea-level variability are also found in the proxy for high-latitude steric variability, while the trend is mainly determined by the combined effects of GIA, present-day mass redistribution and the contribution of high-latitude steric variability. The sum of contributors explains the observed trend and accelerations well within confidence intervals, as well as a large fraction of the decadal sea-level variability.

7. Discussion and Conclusions

We have studied the individual contributors to the observed sea-level trend and decadal sea-level variability along the Northwest Atlantic coast over 1965–2014. The effects of GIA, present-day mass redistribution, and the dynamic signal driven by high-latitude steric variability have been compared to observations of sea level and vertical land motion. For this comparison, we have used a self-consistent framework that takes the difference in observation lengths of GPS and tide gauge records into account. This framework consists of two separate budgets: one for vertical land motion and one for sea level. The vertical land motion that results from present-day mass redistribution (i.e., ice melt, dam retention, and groundwater depletion) is not linear over the full time span of this study. Therefore, a linear trend, estimated over the lengths of the GPS observation is not fully representative for the local long-term vertical land motion. To overcome this problem, we separate the observed VLM into a part explained by GIA and present-day mass redistribution, and an unexplained part. Only the GIA contribution and the unexplained part of the observed VLM are assumed to be linear over the studied period.

GIA causes a complex spatial pattern of land subsidence and sea-level rise in the region: the coast is affected by both uplift from the Laurentide Ice Sheet and by subsidence due to its forebulge collapse. An updated data-driven GIA model is used to explain the tide gauge and GPS observations. With this model, we can explain the observed trends in sea level and vertical land motion to a high extent, as well as the interstation variability of sea-level and VLM trends.

To assess the impact of present-day mass redistribution on regional sea level and land level, we solve the elastic sea-level equation for each mass redistribution process. The effect of ice melt from glaciers and both ice sheets, dam retention, and terrestrial water storage changes due to natural variability and groundwater depletion have been taken into account. The combined mass contribution causes a positive trend and acceleration in both sea level and land motion over our period of interest. The interstation variability in the contribution of present-day mass transport is small.

Model results, altimetry, and hydrographic observations show a strong correlation between steric height in the southern Subpolar Gyre and sea level on the Northwestern Atlantic coast north of Cape Hatteras. This common signal is likely caused by propagation of anomalies in the Labrador Sea, which are propagated southward. The resulting signal causes a positive sea-level trend, explains the large acceleration in observed sea level, and dominates the observed decadal variability along the coast.

Since the Gulf Stream affects coastal sea-level variability south of Cape Hatteras [*McCarthy et al*., 2015], this correlation cannot be observed further south. The observed acceleration in dynamic sea level agrees well with a strong decrease of the water density in the Labrador Sea [*Robson et al*., 2014].

The combination of all these effects allows us to explain the observed station-mean sea-level trend, acceleration, and decadal variability well within the confidence intervals. Observed linear trends at individual tide gauge stations can be explained by the sum of contributors at all stations within the confidence intervals. For 12 out of 14 GPS stations, we can also explain the observed vertical land motion. GIA explains the vast majority of the observed VLM behavior, which causes large interstation differences.

The acceleration in observed sea level in this region is strong, which has already been noted in other studies [e.g., *Sallenger et al*., 2012; *Ezer and Corlett*, 2012]. This strong acceleration is also found in the southern Subpolar Gyre steric observations. However, our 50 year record is too short to separate a secular acceleration from multidecadal variability. It is known that multidecadal variability has a large effect on acceleration estimates from tide gauge records [e.g., *Dangendorf et al*., 2014b; *Haigh et al*., 2014]. In our region, *Kopp* [2013] argues that the observed acceleration does not yet exceed the likely range of multidecadal variability. Hence, the acceleration that we observe in this study may not be representative for longer periods.

Some of the questions that are not yet fully answered in this study are the physical mechanisms behind the high-latitude steric variability and whether other dynamical processes affect decadal sea-level variability, trends and acceleration in the southern Subpolar Gyre and along the coast. Since changes in the density of the Labrador Sea are linked to both changes in the strength of the AMOC and the Deep Western Boundary Current [*Hodson and Sutton*, 2012; *Roberts et al*., 2013], understanding how these mechanisms are linked to coastal sea-level changes may help gaining insight into the impact of AMOC changes and other ocean dynamic processes on coastal sea level. Furthermore, separating the impact of the AMOC from other processes on sea level in this region may aid in improving coastal sea-level projections, which heavily depend on the coupling between expected decline of AMOC strength and higher sea level along the US Atlantic coast.

Acknowledgments

Tide gauge data have been obtained from the Permanent Service for Mean Sea Level (www.psmsl.org). The pressure and wind fields from the twentieth Century Reanalysis Project V2c have been obtained from NOAA Earth System Research Laboratory (www.esrl.noaa.gov/psd/data/gridded). JRA55 reanalysis data have been obtained from the Japan Meteorological Agency (jra.kishou.go.jp/JRA-55/index_en.html). ICOADS 3.0 data have been downloaded from UCAR/NCAR Research Data Archive (rda.ucar.edu/datasets/ds548.0/). The MIDAS GPS velocities have been downloaded from Nevada Geodetic Laboratory (geodesy.unr.edu/). The global ICE6G-VM5a model has been obtained from www.atmosp.physics.utoronto.ca/~peltier/data.php. The altimetry data set from AVISO is distributed by the Copernicus Marine and Environment Monitoring Service (CMEMS) (www.marine.copernicus.eu). EN4 version 4.1.1 gridded temperature and salinity fields were obtained from the U.K. Met Office (www.metoffice.gov.uk/hadobs/en4/). The Hector software package (v1.6) has been downloaded from segal.ubi.pt/hector. All plots were generated using the Generic Mapping Tools. We would also like to thank Ben Marzeion, for providing the regional glacier mass balance data, Kurt H. Kjær and Kristian K. Kjeldsen for providing the Greenland mass balance data, Michiel van den Broeke for the RACMO2.3 SMB data, and Yoshihide Wada for providing the hydrology and dam retention data. This study was funded through the Netherlands Organisation for Scientific Research (NWO) VIDI grant 864.12.012.

References

Andres, M., G. G. Gawarkiewicz, and J. M. Toole (2013), Interannual sea level variability in the western North Atlantic: Regional forcing and remote response, *Geophys. Res. Lett.*, *40*, 5915–5919, doi:10.1002/2013GL058013.

Bamber, J., and R. E. M. Riva (2010), The sea level fingerprint of recent ice mass fluxes, *Cryosphere*, *4*(4), 621–627, doi:10.5194/tc-4-621-2010.

Bingham, R. J., and C. W. Hughes (2009), Signature of the Atlantic meridional overturning circulation in sea level along the east coast of North America, *Geophys. Res. Lett.*, *36*, L02603, doi:10.1029/2008GL036215.

Bingham, R. J., and C. W. Hughes (2012), Local diagnostics to estimate density-induced sea level variations over topography and along coastlines, *J. Geophys. Res.*, *117*, C01013, doi:10.1029/2011JC007276.

Blewitt, G., C. Kreemer, W. C. Hammond, and J. Gazeaux (2016), MIDAS robust trend estimator for accurate GPS station velocities without step detection, *J. Geophys. Res. Solid Earth*, *121*, 2054–2068, doi:10.1002/2015JB012552.

Boon, J. D. (2012), Evidence of sea level acceleration at US and Canadian tide stations, Atlantic Coast, North America, *J. Coastal Res.*, *28*(6), 1437–1445, doi:10.2112/JCOASTRES-D-12-00102.1.

Bos, M. S., R. M. S. Fernandes, S. D. P. Williams, and L. Bastos (2013), Fast error analysis of continuous GNSS observations with missing data, *J. Geod.*, *87*(4), 351–360, doi:10.1007/s00190-012-0605-0.

Bos, M. S., S. D. P. Williams, I. B. Araújo, and L. Bastos (2014), The effect of temporal correlated noise on the sea level rate and acceleration uncertainty, *Geophys. J. Int.*, *196*, 1423–1430, doi:10.1093/gji/ggt481.

Chao, B. F., Y. H. Wu, and Y. S. Li (2008), Impact of artificial reservoir water impoundment on global sea level, *Science*, *320*(5873), 212–214, doi:10.1126/science.1154580.

Compo, G. P., et al. (2011), The twentieth century reanalysis project, *Q. J. R. Meteorol. Soc.*, *137*(654), 1–28, doi:10.1002/qj.776.

Dangendorf, S., F. M. Calafat, A. Arns, T. Wahl, I. D. Haigh, and J. Jensen (2014a), Mean sea level variability in the North Sea: Processes and implications, *J. Geophys. Res. Oceans*, *119*, 6820–6841, doi:10.1002/2014JC009901.

Dangendorf, S., D. Rybski, C. Mudersbach, A. Müller, E. Kaufmann, E. Zorita, and J. Jensen (2014b), Evidence for long-term memory in sea level, *Geophys. Res. Lett.*, *41*, 5530–5537, doi:10.1002/2014GL060538.

Davis, J. L., and J. X. Mitrovica (1996), Glacial isostatic adjustment and the anomalous tide gauge record of eastern North America, *Nature*, *379*(6563), 331–333, doi:10.1038/379331a0.

Engelhart, S. E., B. P. Horton, B. C. Douglas, W. R. Peltier, and T. E. Törnqvist (2009), Spatial variability of late Holocene and 20th century sea-level rise along the Atlantic coast of the United States, *Geology*, *37*(12), 1115–1118, doi:10.1130/G30360A.1.

Ezer, T. (2013), Sea level rise, spatially uneven and temporally unsteady: Why the U.S. East Coast, the global tide gauge record, and the global altimeter data show different trends, *Geophys. Res. Lett.*, *40*, 5439–5444, doi:10.1002/2013GL057952.

Ezer, T., and W. B. Corlett (2012), Is sea level rise accelerating in the Chesapeake Bay? A demonstration of a novel new approach for analyzing sea level data, *Geophys. Res. Lett.*, *39*, L19605, doi:10.1029/2012GL053435.

Farrell, W. E., and J. A. Clark (1976), On postglacial sea level, *Geophys. J. Int.*, *46*(3), 647–667, doi:10.1111/j.1365-246X.1976.tb01252.x.

Fischer, J., F. A. Schott, and M. Dengler (2004), Boundary circulation at the exit of the Labrador Sea, *J. Phys. Oceanogr.*, *34*(7), 1548–1570, doi:10.1175/1520-0485(2004)034 < 1548:BCATEO>2.0.CO;2.

Frederikse, T., R. Riva, M. Kleinherenbrink, Y. Wada, M. van den Broeke, and B. Marzeion (2016), Closing the sea level budget on a regional scale: Trends and variability on the Northwestern European continental shelf, *Geophys. Res. Lett.*, *43*, 10,864–10,872, doi:10.1002/2016GL070750.

Freeman, E., et al. (2016), ICOADS Release 3.0: A major update to the historical marine climate record, *Int. J. Climatol.*, *37*, 2211–2232, doi:10.1002/joc.4775.

Gazeaux, J., et al. (2013), Detecting offsets in GPS time series: First results from the detection of offsets in GPS experiment, *J. Geophys. Res. Solid Earth*, *118*, 2397–2407, doi:10.1002/jgrb.50152.

Good, S. A., M. J. Martin, and N. A. Rayner (2013), EN4: Quality controlled ocean temperature and salinity profiles and monthly objective analyses with uncertainty estimates, *J. Geophys. Res. Oceans*, *118*, 6704–6716, doi:10.1002/2013JC009067.

Gouretski, V., and F. Reseghetti (2010), On depth and temperature biases in bathythermograph data: Development of a new correction scheme based on analysis of a global ocean database, *Deep Sea Res., Part I*, *57*(6), 812–833, doi:10.1016/j.dsr.2010.03.011.

Haigh, I. D., T. Wahl, E. J. Rohling, R. M. Price, C. B. Pattiaratchi, F. M. Calafat, and S. Dangendorf (2014), Timescales for detecting a significant acceleration in sea level rise, *Nat. Commun.*, *5*, Article 3635, doi:10.1038/ncomms4635.

Häkkinen, S. (2001), Variability in sea surface height: A qualitative measure for the meridional overturning in the North Atlantic, *J. Geophys. Res.*, *106*(C7), 13,837–13,848, doi:10.1029/1999JC000155.

Han, G., K. Ohashi, N. Chen, P. G. Myers, N. Nunes, and J. Fischer (2010), Decline and partial rebound of the Labrador Current 1993–2004: Monitoring ocean currents from altimetric and conductivity-temperature-depth data, *J. Geophys. Res.*, *115*, C12012, doi:10.1029/2009JC006091.

Han, G., Z. Ma, H. Bao, and A. Slangen (2014), Regional differences of relative sea level changes in the Northwest Atlantic: Historical trends and future projections, *J. Geophys. Res. Oceans*, *119*, 156–164, doi:10.1002/2013JC009454.

Hodson, D. L. R., and R. T. Sutton (2012), The impact of resolution on the adjustment and decadal variability of the Atlantic meridional overturning circulation in a coupled climate model, *Clim. Dyn.*, *39*(12), 3057–3073, doi:10.1007/s00382-012-1309-0.

Holgate, S. J., A. Matthews, P. L. Woodworth, L. J. Rickards, M. E. Tamisiea, E. Bradshaw, P. R. Foden, K. M. Gordon, S. Jevrejeva, and J. Pugh (2013), New data systems and products at the permanent service for mean sea level, *J. Coastal Res.*, *29*(3), 493–504, doi:10.2112/JCOASTRES-D-12-00175.1.

Hsieh, W. W., and K. Bryan (1996), Redistribution of sea level rise associated with enhanced greenhouse warming: A simple model study, *Clim. Dyn.*, *12*(8), 535–544, doi:10.1007/BF00207937.

Hughes, C. W., and M. P. Meredith (2006), Coherent sea-level fluctuations along the global continental slope, *Philos. Trans. R. Soc. A*, *364*(1841), 885–901, doi:10.1098/rsta.2006.1744.

Huthnance, J. M. (1978), On coastal trapped waves: Analysis and numerical calculation by inverse iteration, *J. Phys. Oceanogr.*, *8*(1), 74–92, doi:10.1175/1520-0485(1978)008 < 0074:OCTWAA>2.0.CO;2.

Johnson, H. L., and D. P. Marshall (2002), A theory for the surface Atlantic response to thermohaline variability, *J. Phys. Oceanogr.*, *32*(4), 1121–1132, doi:10.1175/1520-0485(2002)032 < 1121:ATFTSA>2.0.CO;2.

Karegar, M. A., T. H. Dixon, and S. E. Engelhart (2016), Subsidence along the Atlantic Coast of North America: Insights from GPS and late Holocene relative sea level data, *Geophys. Res. Lett.*, *43*, 3126–3133, doi:10.1002/2016GL068015.

Kieke, D., and I. Yashayaev (2015), Studies of Labrador Sea Water formation and variability in the subpolar North Atlantic in the light of international partnership and collaboration, *Prog. Oceanogr.*, *132*, 220–232, doi:10.1016/j.pocean.2014.12.010.

Kjeldsen, K. K., et al. (2015), Spatial and temporal distribution of mass loss from the Greenland Ice Sheet since AD 1900, *Nature*, *528*(7582), 396–400, doi:10.1038/nature16183.

Kobayashi, S., et al. (2015), The JRA-55 reanalysis: General specifications and basic characteristics, *J. Meteorol. Soc. Jpn.*, *93*(1), 5–48, doi:10.2151/jmsj.2015-001.

Kopp, R. E. (2013), Does the mid-Atlantic United States sea level acceleration hot spot reflect ocean dynamic variability?, *Geophys. Res. Lett.*, *40*, 3981–3985, doi:10.1002/grl.50781.

Landerer, F. W., J. H. Jungclaus, and J. Marotzke (2007), Regional dynamic and steric sea level change in response to the IPCC-A1B scenario, *J. Phys. Oceanogr.*, *37*(2), 296–312, doi:10.1175/JPO3013.1.

Lehner, B., et al. (2011), High-resolution mapping of the world's reservoirs and dams for sustainable river-flow management, *Frontiers Ecol. Environ.*, *9*(9), 494–502, doi:10.1890/100125.

Li, Y., R. Ji, P. S. Fratantoni, C. Chen, J. A. Hare, C. S. Davis, and R. C. Beardsley (2014), Wind-induced interannual variability of sea level slope, along-shelf flow, and surface salinity on the Northwest Atlantic shelf, *J. Geophys. Res. Oceans*, *119*, 2462–2479, doi:10.1002/2013JC009385.

Marzeion, B., P. W. Leclercq, J. G. Cogley, and A. H. Jarosch (2015), Brief communication: Global reconstructions of glacier mass change during the 20th century are consistent, *Cryosphere*, *9*(6), 2399–2404, doi:10.5194/tc-9-2399-2015.
McCarthy, G. D., I. D. Haigh, J. J.-M. Hirschi, J. P. Grist, and D. A. Smeed (2015), Ocean impact on decadal Atlantic climate variability revealed by sea-level observations, *Nature*, *521*(7553), 508–510, doi:10.1038/nature14491.
Mitrovica, J. X., C. C. Hay, E. Morrow, R. E. Kopp, M. Dumberry, and S. Stanley (2015), Reconciling past changes in Earth's rotation with 20th century global sea-level rise: Resolving Munks enigma, *Sci. Adv.*, *1*(11), e1500679, doi:10.1126/sciadv.1500679.
Noël, B., W. J. van de Berg, E. van Meijgaard, P. K. Munneke, R. S. W. van de Wal, and M. R. van den Broeke (2015), Evaluation of the updated regional climate model RACMO2.3: Summer snowfall impact on the Greenland Ice Sheet, *Cryosphere*, *9*(5), 1831–1844, doi:10.5194/tc-9-1831-2015.
Peltier, W. R., D. F. Argus, and R. Drummond (2015), Space geodesy constrains ice age terminal deglaciation: The global ICE-6G_C (VM5a) model, *J. Geophys. Res. Solid Earth*, *120*, 450–487, doi:10.1002/2014JB011176.
Piecuch, C. G., and R. M. Ponte (2015), Inverted barometer contributions to recent sea level changes along the northeast coast of North America, *Geophys. Res. Lett.*, *42*, 5918–5925, doi:10.1002/2015GL064580.
Piecuch, C. G., S. Dangendorf, R. M. Ponte, and M. Marcos (2016), Annual sea level changes on the North American Northeast coast: Influence of local winds and barotropic motions, *J. Clim.*, *29*(2016), 4801–4816, doi:10.1175/JCLI-D-16-0048.1.
Rhein, M., D. Kieke, S. Hüttl-Kabus, A. Roessler, C. Mertens, R. Meissner, B. Klein, C. W. Böning, and I. Yashayaev (2011), Deep water formation, the subpolar gyre, and the meridional overturning circulation in the subpolar North Atlantic, *Deep Sea Res., Part II*, *58*(17), 1819–1832, doi:10.1016/j.dsr2.2010.10.061.
Roberts, C. D., F. K. Garry, and L. C. Jackson (2013), A multimodel study of sea surface temperature and subsurface density fingerprints of the Atlantic meridional overturning circulation, *J. Clim.*, *26*(22), 9155–9174, doi:10.1175/JCLI-D-12-00762.1.
Robson, J., D. Hodson, E. Hawkins, and R. Sutton (2014), Atlantic overturning in decline?, *Nat. Geosci.*, *7*(1), 2–3, doi:10.1038/ngeo2050.
Roquet, F., G. Madec, T. J. McDougall, and P. M. Barker (2015), Accurate polynomial expressions for the density and specific volume of seawater using the TEOS-10 standard, *Ocean Modell.*, *90*, 29–43, doi:10.1016/j.ocemod.2015.04.002.
Roussenov, V. M., R. G. Williams, C. W. Hughes, and R. J. Bingham (2008), Boundary wave communication of bottom pressure and overturning changes for the North Atlantic, *J. Geophys. Res.*, *113*, C08042, doi:10.1029/2007JC004501.
Roy, K., and W. R. Peltier (2015), Glacial isostatic adjustment, relative sea level history and mantle viscosity: Reconciling relative sea level model predictions for the U.S. East coast with geological constraints, *Geophys. J. Int.*, *201*(2), 1156–1181, doi:10.1093/gji/ggv066.
Sabadini, R., B. Vermeersen, and G. Cambiotti (2016), *Global Dynamics of the Earth: Applications of Viscoelastic Relaxation Theory to Solid-Earth and Planetary Geophysics*, Springer, Dordrecht, Netherlands, doi:10.1007/978-94-017-7552-6-2.
Sallenger, A. H., K. S. Doran, and P. A. Howd (2012), Hotspot of accelerated sea-level rise on the Atlantic coast of North America, *Nat. Clim. Change*, *2*(12), 884–888, doi:10.1038/nclimate1597.
Santamaría-Gómez, A., and A. Mémin (2015), Geodetic secular velocity errors due to interannual surface loading deformation, *Geophys. J. Int.*, *202*(2), 763–767, doi:10.1093/gji/ggv190.
Santamaría-Gómez, A., M. Gravelle, X. Collilieux, M. Guichard, B. M. Míguez, P. Tiphaneau, and G. Wöppelmann (2012), Mitigating the effects of vertical land motion in tide gauge records using a state-of-the-art GPS velocity field, *Global Planet. Change*, *98*, 6–17, doi:10.1016/j.gloplacha.2012.07.007.
Shepherd, A., et al. (2012), A reconciled estimate of ice-sheet mass balance, *Science*, *338*(6111), 1183–1189, doi:10.1126/science.1228102.
Simon, K. M., and R. E. M. Riva (2016), A data-driven model of present-day glacial isostatic adjustment in North America, *Geophys. Res. Abstr.*, *18*, 1, doi:10.13140/RG.2.2.13343.76964.
Stammer, D., A. Cazenave, R. M. Ponte, and M. E. Tamisiea (2013), Causes for contemporary regional sea level changes, *Annu. Rev. Mar. Sci.*, *5*, 21–46, doi:10.1146/annurev-marine-121211-172406.
Tamisiea, M. E. (2011), Ongoing glacial isostatic contributions to observations of sea level change, *Geophys. J. Int.*, *186*(3), 1036–1044, doi:10.1111/j.1365-246X.2011.05116.x.
Tamisiea, M. E., and J. X. Mitrovica (2011), The moving boundaries of sea level change understanding the origins of geographic variability, *Oceanography*, *24*(2), 24–39, doi:10.5670/oceanog.2011.25.
Tamisiea, M. E., E. M. Hill, R. M. Ponte, J. L. Davis, I. Velicogna, and N. T. Vinogradova (2010), Impact of self-attraction and loading on the annual cycle in sea level, *J. Geophys. Res.*, *115*, C07004, doi:10.1029/2009JC005687.
Thompson, K. R. (1986), North Atlantic sea-level and circulation, *Geophys. J. Int.*, *87*(1), 15–32, doi:10.1111/j.1365-246X.1986.tb04543.x.
Thompson, P. R., and G. T. Mitchum (2014), Coherent sea level variability on the North Atlantic western boundary, *J. Geophys. Res. Oceans*, *119*, 5676–5689, doi:10.1002/2014JC009999.
van den Broeke, M. R., E. M. Enderlin, I. M. Howat, P. K. Munneke, B. P. Y. Noël, W. J. van de Berg, E. van Meijgaard, and B. Wouters (2016), On the recent contribution of the Greenland ice sheet to sea level change, *Cryosphere*, *10*(5), 1933–1946, doi:10.5194/tc-10-1933-2016.
van Wessem, J. M., et al. (2014), Improved representation of East Antarctic surface mass balance in a regional atmospheric climate model, *J. Glaciol.*, *60*(222), 761–770, doi:10.3189/2014JoG14J051.
Veit, E., and C. P. Conrad (2016), The impact of groundwater depletion on spatial variations in sea level change during the past century, *Geophys. Res. Lett.*, *43*, 3351–3359, doi:10.1002/2016GL068118.
Wada, Y., L. P. H. van Beek, and M. F. P. Bierkens (2011), Modelling global water stress of the recent past: On the relative importance of trends in water demand and climate variability, *Hydrol. Earth Syst. Sci.*, *15*(12), 3785–3808, doi:10.5194/hess-15-3785-2011.
Wada, Y., D. Wisser, and M. F. P. Bierkens (2014), Global modeling of withdrawal, allocation and consumptive use of surface water and groundwater resources, *Earth Syst. Dyn.*, *5*(1), 15–40, doi:10.5194/esd-5-15-2014.
Watkins, M. M., D. N. Wiese, D.-N. Yuan, C. Boening, and F. W. Landerer (2015), Improved methods for observing Earth's time variable mass distribution with GRACE using spherical cap mascons, *J. Geophys. Res. Solid Earth*, *120*, 2648–2671, doi:10.1002/2014JB011547.
Woodworth, P. L. (2012), A note on the nodal tide in sea level records, *J. Coastal Res.*, *28*(2), 316–323, doi:10.2112/JCOASTRES-D-11A-00023.1.
Woodworth, P. L., M. Á. M. Maqueda, V. M. Roussenov, R. G. Williams, and C. W. Hughes (2014), Mean sea-level variability along the northeast American Atlantic coast and the roles of the wind and the overturning circulation, *J. Geophys. Res. Oceans*, *119*, 8916–8935, doi:10.1002/2014JC010520.
Wöppelmann, G., and M. Marcos (2016), Vertical land motion as a key to understanding sea level change and variability, *Rev. Geophys.*, *54*, 64–92, doi:10.1002/2015RG000502.
Yin, J., M. E. Schlesinger, and R. J. Stouffer (2009), Model projections of rapid sea-level rise on the northeast coast of the United States, *Nat. Geosci.*, *2*(4), 262–266, doi:10.1038/ngeo462.